

Dense dislocations enable high-performance PbSe thermoelectric at low-medium temperatures

Received: 15 September 2022

Accepted: 19 October 2022

Published online: 28 October 2022

Check for updates

Liqing Xu¹, Yu Xiao¹✉, Sining Wang², Bo Cui³✉, Di Wu⁴,
Xiangdong Ding¹ & Li-Dong Zhao²✉

PbSe-based thermoelectric materials exhibit promising ZT values at medium temperature, but its near-room-temperature thermoelectric properties are overlooked, thus restricting its average ZT (ZT_{ave}) value at low-medium temperatures. Here, a high ZT_{ave} of 0.90 at low temperature (300–573 K) is reported in n -type PbSe-based thermoelectric material ($\text{Pb}_{1.02}\text{Se}_{0.72}\text{Te}_{0.20}\text{S}_{0.08}\text{-0.3\%Cu}$), resulting in a large ZT_{ave} of 0.96 at low-medium temperatures (300–773 K). This high thermoelectric performance stems from its ultralow lattice thermal conductivity caused by dense dislocations through heavy Te/S alloying and Cu interstitial doping. The dislocation density evaluated by modified Williamson-Hall method reaches up to $5.4 \times 10^{16} \text{ m}^{-2}$ in $\text{Pb}_{1.02}\text{Se}_{0.72}\text{Te}_{0.20}\text{S}_{0.08}\text{-0.3\%Cu}$. Moreover, the microstructure observation further uncovers two kinds of dislocations, namely screw and edge dislocations, with several to hundreds of nanometers scale in length. These dislocations in lattice can strongly intensify phonon scattering to minimize the lattice thermal conductivity and simultaneously maintain high carrier transport. As a result, with the reduced lattice thermal conductivity and optimized power factor in $\text{Pb}_{1.02}\text{Se}_{0.72}\text{Te}_{0.20}\text{S}_{0.08}\text{-0.3\%Cu}$, its near-room-temperature thermoelectric performance is largely enhanced and exceeds previous PbSe-based thermoelectric materials.

Thermoelectric (TE) materials have the ability to realize direct conversion between waste heat and electricity, which can ease the energy and environment crisis^{1–4}. The energy conversion efficiency of thermoelectric devices depends on the dimensionless figure of merit (ZT), $ZT = S^2\sigma T/\kappa_{\text{tot}}$, where S , σ , T , κ_{tot} denote Seebeck coefficient, electrical conductivity, absolute temperature in kelvin and the total thermal conductivity, respectively. Notably, the key to develop high-performance TE materials is decoupling these inter-dependent TE parameters to improve power factor $PF = S^2\sigma$ or reduce κ_{tot} , where κ_{tot} is a sum of electronic thermal conductivity (κ_{ele}) and lattice thermal conductivity (κ_{lat})^{5–7}.

Lead chalcogenides are good thermoelectric materials, and many advanced strategies to optimize thermoelectric performance have been developed based on lead chalcogenides, especially for PbTe, such as band convergence^{8,9}, resonant state^{10,11}, nanostructuring^{12–16}, etc. Among lead chalcogenides, PbSe thermoelectric material is a promising alternative of PbTe due to its low-cost Se element and balanced carrier and phonon transport properties. To enhance the thermoelectric performance in PbSe, some effective approaches have recently been reported, including band flattening to improve carrier effective mass^{17–19}, band sharpening to tune carrier mobility^{20,21},

¹State Key Laboratory for Mechanical Behavior of Materials, Xi'an Jiaotong University, 710049 Xi'an, China. ²School of Materials Science and Engineering, Beihang University, 100191 Beijing, China. ³Institute of Nuclear Physics and Chemistry, China Academy of Engineering Physics, 621900 Mianyang, China. ⁴School of Materials Science and Engineering, Shaanxi Normal University, 710049 Xi'an, China. ✉e-mail: xiao_yu@xjtu.edu.cn; cuiibo13@163.com; zhaolidong@buaa.edu.cn

dynamic doping to optimize carrier density^{20,22}, defects design to scatter phonon transport^{23–25}, etc. Notably, it is found that the vacancy or interstitial-induced dislocations in PbSe-based thermoelectric material can largely reduce the lattice thermal conductivity while causing little effect on electrical transport properties, thus finally enhancing the peak ZT value. However, the dislocation strategies in previous works fail to optimize the near-room-temperature thermoelectric performance, and its average ZT value at low-medium temperatures maintains at low value, which might be caused by the low dislocation density to intensify phonon scattering at low temperature range. Therefore, to further enhance the thermoelectric performance in PbSe at low-medium temperatures, this work aims to produce dense dislocations in PbSe lattice in order to substantially suppress the lattice thermal conductivity.

In fact, the dislocation produced by only vacancy^{26–28} or interstitial^{22,29,30} is limited to their solubility in matrix, which makes it challengeable to achieve high dislocation density ($N_D > 10^{15} \text{ m}^{-2}$) in thermoelectric materials. Herein, this work firstly introduces heavily Te and S alloying in PbSe matrix so as to cause strong lattice distortion, which can provide extra energy for dislocation formation. And then, based on the optimal Te and S co-alloyed $\text{Pb}_{1.02}\text{Se}_{0.72}\text{Te}_{0.20}\text{S}_{0.08}$ sample, the Cu interstitial doping is imported to accelerate dislocation formation. With these two successive steps, very high dislocation density of $5.4 \times 10^{16} \text{ m}^{-2}$ can be obtained in $\text{Pb}_{1.02}\text{Se}_{0.72}\text{Te}_{0.20}\text{S}_{0.08}-0.3\% \text{ Cu}$, which is much higher than that in previously reported n -type PbSe-based samples. Such dense dislocations in $\text{Pb}_{1.02}\text{Se}_{0.72}\text{Te}_{0.20}\text{S}_{0.08}-0.3\% \text{ Cu}$ contributes to ultralow lattice thermal conductivity in the whole-temperature range. Moreover, its room-temperature lattice thermal conductivity can be reduced to $0.42 \text{ W m}^{-1} \text{ K}^{-1}$ and the minimal lattice thermal conductivity reaches at $0.29 \text{ W m}^{-1} \text{ K}^{-1}$ at 573 K. Additionally, these dislocations in matrix play slight impact on carrier transport and can maintain a decent weighted carrier mobility. Eventually, the thermoelectric performance is substantially enhanced in $\text{Pb}_{1.02}\text{Se}_{0.72}\text{Te}_{0.20}\text{S}_{0.08}-x\% \text{ Cu}$ ($x = 0-0.40$) at low-medium temperatures, and a room-temperature ZT value of 0.62 and ZT_{ave} of 0.90 at 300–573 K can be realized in $\text{Pb}_{1.02}\text{Se}_{0.72}\text{Te}_{0.20}\text{S}_{0.08}-0.3\% \text{ Cu}$.

Results

To obtain high thermoelectric performance in n -type PbSe-based material at low-medium temperatures, this work aims to import dense dislocations to substantially reduce the lattice thermal conductivity. Firstly, over-stoichiometric Pb atoms are used to realize electron dominated n -type $\text{Pb}_{1.02}\text{Se}$. Then, Te and S alloying in $\text{Pb}_{1.02}\text{Se}$ are following introduced to cause lattice distortion, which is favorable for dislocation formation, and also results in strong strain field to reduce lattice thermal conductivity. Finally, Cu interstitial doping in $\text{Pb}_{1.02}\text{Se}_{0.72}\text{Te}_{0.20}\text{S}_{0.08}$ promotes the dislocation formation, and high dislocation density in $\text{Pb}_{1.02}\text{Se}_{0.72}\text{Te}_{0.20}\text{S}_{0.08}-0.3\% \text{ Cu}$ is revealed by microstructure observation. These dense dislocations largely reduce the lattice thermal conductivity and lead to high thermoelectric performance at low-medium temperatures in n -type $\text{Pb}_{1.02}\text{Se}_{0.72}\text{Te}_{0.20}\text{S}_{0.08}-0.3\% \text{ Cu}$.

Crystal structure identification and lattice thermal conductivity

The powder XRD patterns of $\text{Pb}_{1.02}\text{Se}_{1-x}\text{Te}_x$ ($x = 0-0.20$) and $\text{Pb}_{1.02}\text{Se}_{1-y}\text{S}_y$ ($y = 0-0.10$) can be completely indexed as the rock-salt structure (Fig. 1a, b), and with rising Te/S alloying content, lattice expansion and contraction are clearly observed in Te-alloyed PbSe and S-alloyed PbSe samples, respectively. Moreover, the lattice parameter of 6.12 Å in $\text{Pb}_{1.02}\text{Se}$ linearly increases to 6.17 Å in $\text{Pb}_{1.02}\text{Se}_{0.8}\text{Te}_{0.2}$ and decreases to 6.10 Å in $\text{Pb}_{1.02}\text{Se}_{0.9}\text{S}_{0.1}$ (Fig. 1c). As a result, the room-temperature lattice thermal conductivity of $\text{Pb}_{1.02}\text{Se}_{1-x}\text{Te}_x$ ($x = 0-0.20$) and $\text{Pb}_{1.02}\text{Se}_{1-y}\text{S}_y$ ($y = 0-0.10$) show significant decrease from $1.68 \text{ W m}^{-1} \text{ K}^{-1}$ in $\text{Pb}_{1.02}\text{Se}$ to $0.69 \text{ W m}^{-1} \text{ K}^{-1}$ in $\text{Pb}_{1.02}\text{Se}_{0.8}\text{Te}_{0.2}$ and $1.18 \text{ W m}^{-1} \text{ K}^{-1}$ in $\text{Pb}_{1.02}\text{Se}_{0.92}\text{S}_{0.08}$ (Fig. 1d). The origin of diminished

lattice thermal conductivity in $\text{Pb}_{1.02}\text{Se}_{1-x}\text{Te}_x$ ($x = 0-0.20$) and $\text{Pb}_{1.02}\text{Se}_{1-y}\text{S}_y$ ($y = 0-0.10$) stems from the lattice distortion after alloying, which can intensify phonon scattering due to mass and strain field fluctuations in matrix lattice. As the heavy Te/S alloying in n -type PbSe not only scatters phonon but also blocks carrier transport, no enhancement of ZT value can be obtained in $\text{Pb}_{1.02}\text{Se}_{1-x}\text{Te}_x$ ($x = 0-0.20$) and $\text{Pb}_{1.02}\text{Se}_{1-y}\text{S}_y$ ($y = 0-0.10$) samples (Supplementary Fig. 1–4).

Based on the minimal thermal conductivity in Te/S-alloyed PbSe, Cu interstitial doping is introduced into $\text{Pb}_{1.02}\text{Se}_{0.72}\text{Te}_{0.20}\text{S}_{0.08}$. With these successive steps, the lattice thermal conductivity in this work is largely suppressed (Fig. 2a). The room-temperature lattice thermal conductivity is suppressed from $1.68 \text{ W m}^{-1} \text{ K}^{-1}$ in $\text{Pb}_{1.02}\text{Se}$ to $0.65 \text{ W m}^{-1} \text{ K}^{-1}$ in $\text{Pb}_{1.02}\text{Se}_{0.72}\text{Te}_{0.20}\text{S}_{0.08}$, and further decreased to $0.42 \text{ W m}^{-1} \text{ K}^{-1}$ in $\text{Pb}_{1.02}\text{Se}_{0.72}\text{Te}_{0.20}\text{S}_{0.08}-0.3\% \text{ Cu}$. Moreover, the temperature-dependent lattice thermal conductivity in $\text{Pb}_{1.02}\text{Se}_{0.72}\text{Te}_{0.20}\text{S}_{0.08}-0.3\% \text{ Cu}$ can maintain at very low value ($< 0.5 \text{ W m}^{-1} \text{ K}^{-1}$) in the whole-temperature range (Fig. 2b), which is comparable with other advanced n -type PbSe, especially at 300–573 K, including PbSe-SnS-Cu²⁰, PbSe-Ag-Sb³¹, PbSe-Cu-Te³⁰, high-entropy PbSe³², PbSe-Cu²², PbSe-Sb-GeSe²⁴. It is worth noting that the theoretical limit of lattice thermal conductivity in PbSe compound is $0.38 \text{ W m}^{-1} \text{ K}^{-1}$ based on the assumption of minimal phonon mean free path^{24,33}. However, some lower lattice thermal conductivity can also be obtained in experimental results, especially in Cu-contained samples, which is closely related to the abnormal Cu atom diffusion with increasing temperature. In fact, some Ag/Cu-based compounds can achieve ultralow lattice thermal conductivity due to the highly mobile Ag/Cu atoms³⁴, indicating that evaluating the theoretical lattice thermal conductivity should further consider the roles of atom diffusion in thermoelectric materials³⁵.

Dislocation density estimation with modified Williamson-Hall (MWH) method

After Cu interstitial doping in $\text{Pb}_{1.02}\text{Se}_{0.72}\text{Te}_{0.20}\text{S}_{0.08}-x\% \text{ Cu}$ ($x = 0-0.40$), all samples still maintain cubic phase and the lattice slightly expands with increasing Cu content, proving the Cu interstitials in matrix (Supplementary Fig. 5). The room-temperature lattice thermal conductivity in $\text{Pb}_{1.02}\text{Se}_{1-x}\text{Te}_x$ ($x = 0-0.2$) and $\text{Pb}_{1.02}\text{Se}_{1-x}\text{S}_x$ ($x = 0-0.1$) can well follow the predicted value by Callaway model (Fig. 3a and Supplementary Table 1). After Cu interstitial doping, the lattice thermal conductivity continuously decreases and begins to deviate from the predicted value. The large deviation of lattice thermal conductivity between experiment result and predicted value suggests extra effects on phonon scattering. As Cu interstitials incline to aggregate and could form line defects in matrix, the modified Williamson-Hall (MWH) method is used to estimate dislocation density. Based on XRD diffraction peak broadening effect, the MWH method for calculating dislocation density derived from Ungár and Borbély can be written as follows when ignore the non-interpreted high-order error terms O^{36-38} :

$$\Delta K = 0.9/d + (\pi A^2 b^2 / 2)^{1/2} N_D^{1/2} (K \bar{C}^{1/2}) \quad (1)$$

where $K = 2 \sin \theta / \lambda$, $\Delta K = 2 \cos \theta (\Delta \theta) / \lambda$, θ and λ are the diffraction angle and the wavelength of X-rays, d is the average grain size, b is the magnitude of Burgers vector and N_D is dislocation density. The derivation of the equation is shown in Supporting Information.

The estimation of dislocation density is divided into three steps. First, the line profiles were fitted by Gaussian function method to obtain the exact Bragg position and full width at half maximum (FWHM). Six diffraction angles are selected for $K - \Delta K$ plot (Fig. 3b), and corresponding indices of crystal plane and FWHM are listed in Supplementary Table 2. The value of $0.9/d$ is obtained by linear fitting. Then, calculating the value of $(\Delta K - 0.9/d)^2 / K^2$, and the value of q is

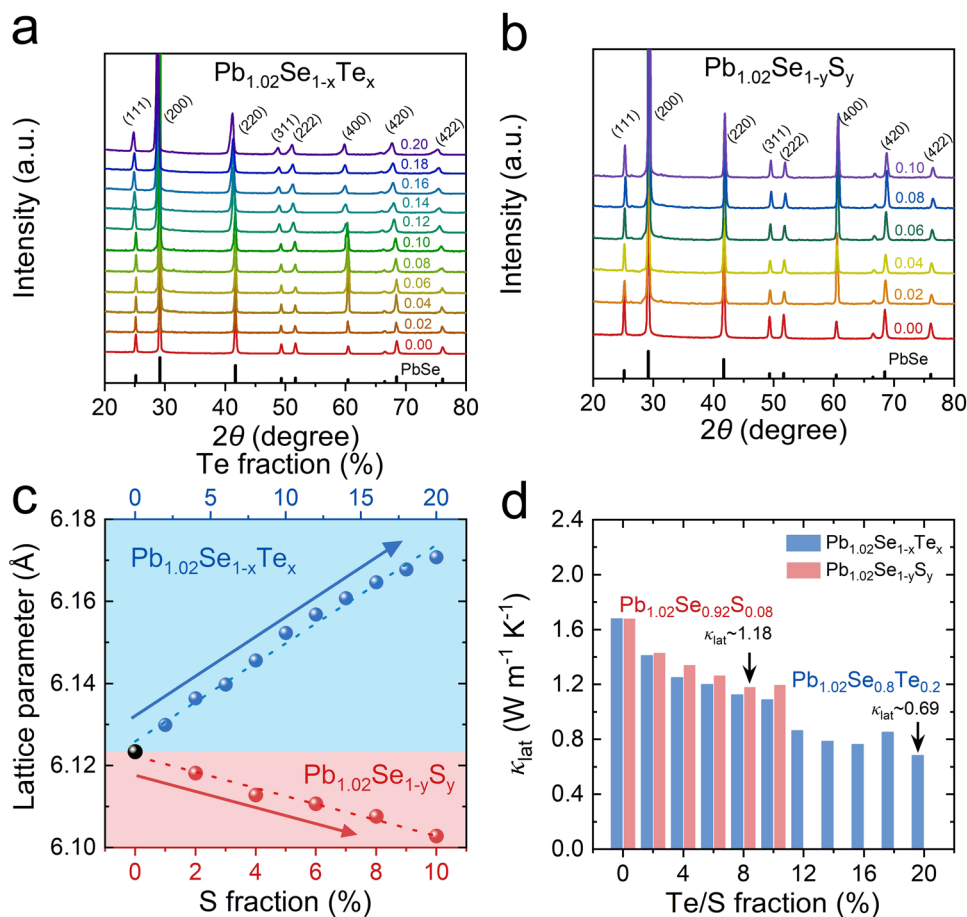


Fig. 1 | PXRD and lattice thermal conductivity of $\text{Pb}_{1.02}\text{Se}_{1-x}\text{Te}_x$ and $\text{Pb}_{1.02}\text{Se}_{1-y}\text{S}_y$. **a** Powder XRD patterns of $\text{Pb}_{1.02}\text{Se}_{1-x}\text{Te}_x$ ($x = 0-0.20$). **b** Powder XRD patterns of $\text{Pb}_{1.02}\text{Se}_{1-y}\text{S}_y$ ($y = 0-0.10$). **c** Lattice parameter as a function of Te/S

fraction. **d** Room-temperature lattice thermal conductivity as a function of Te/S fraction in $\text{Pb}_{1.02}\text{Se}_{1-x}\text{Te}_x$ ($x = 0-0.20$) and $\text{Pb}_{1.02}\text{Se}_{1-y}\text{S}_y$ ($y = 0-0.10$).

obtained by fitting formula of $(\Delta K - 0.9/d)^2/K^2 - H^2$ as follows:

$$\frac{(\Delta K - 0.9/d)^2}{K^2} = (\pi A^2 b^2 / 2) N_D \bar{C}_{h00} (1 - qH^2) \quad (2)$$

where the calculated q equals -1.46 (Fig. 3c). The \bar{C} of different crystal plane is obtained by equation (S29). Finally, the dislocation density can be calculated by the slope of the $\Delta K - KC^{1/2}$ plot in Eq. (1) (Fig. 3d), the details of other parameters are listed in Supplementary Table 3. Moreover, the final dislocation density in $\text{Pb}_{1.02}\text{Se}_{0.72}\text{Te}_{0.20}\text{S}_{0.08}-0.3\%$ Cu can reach up to $5.4 \times 10^{16} \text{ m}^{-2}$, which is much higher than that in other lead chalcogenides, such as N_D of $5 \times 10^{12} \text{ m}^{-2}$ in n -type $\text{Pb}_{0.95}\text{Sb}_{0.33}\text{Se}^{26}$, N_D of $3 \times 10^{15} \text{ m}^{-2}$ in n -type $\text{Pb}_{0.95}\text{Sb}_{0.33}\text{Se}_{0.6}\text{Te}_{0.4}^{39}$, N_D of $4 \times 10^{12} \text{ m}^{-2}$ in p -type $\text{Na}_{0.025}\text{Eu}_{0.03}\text{Pb}_{0.945}\text{Te}^{40}$, and N_D of $2 \times 10^{14} \text{ m}^{-2}$ (grain interior) and $1 \times 10^{16} \text{ m}^{-2}$ (grain boundary) in PbTe-Ag^{41} . The high dislocation density in $\text{Pb}_{1.02}\text{Se}_{0.72}\text{Te}_{0.20}\text{S}_{0.08}-0.3\%$ Cu is ascribed to the strong lattice distortion caused by heavy Te/S alloying and Cu interstitial doping. Compared with $\text{Pb}_{1.02}\text{Se}_{0.72}\text{Te}_{0.20}\text{S}_{0.08}$ sample (Supplementary Table 2 and Supplementary Fig. 6), $\text{Pb}_{1.02}\text{Se}_{0.72}\text{Te}_{0.20}\text{S}_{0.08}-0.3\%$ Cu owns larger value of FWHM, thus resulting in higher dislocation density. Additionally, this result indicates that Cu interstitial can further promote dislocation formation and indirectly proves a lower dislocation formation energy in $\text{Pb}_{1.02}\text{Se}_{0.72}\text{Te}_{0.20}\text{S}_{0.08}-0.3\%$ Cu than that in $\text{Pb}_{1.02}\text{Se}_{0.72}\text{Te}_{0.20}\text{S}_{0.08}$.

Microstructure observations in $\text{Pb}_{1.02}\text{Se}_{0.72}\text{Te}_{0.20}\text{S}_{0.08}-0.3\%$ Cu
To directly see the dislocation in matrix, the scanning transmission electron microscopy (STEM) is carried out. Large-scale

dislocation networks form in $\text{Pb}_{1.02}\text{Se}_{0.72}\text{Te}_{0.20}\text{S}_{0.08}-0.3\%$ Cu from low-magnification TEM image (Fig. 4a), and the matrix still preserves cubic PbSe-based phase from electron diffraction pattern inset. In medium-magnification STEM ABF image (Fig. 4b), dense dislocations can be clearly observed and both edge and screw dislocations exist in $\text{Pb}_{1.02}\text{Se}_{0.72}\text{Te}_{0.20}\text{S}_{0.08}-0.3\%$ Cu. By counting the local dislocation, the estimated total dislocation density is around $6.4 \times 10^{16} \text{ m}^{-2}$, which is consistent with the modified Williamson-Hall results above. The statistical results further reveal 75% edge dislocation and 25% screw dislocation in $\text{Pb}_{1.02}\text{Se}_{0.72}\text{Te}_{0.20}\text{S}_{0.08}-0.3\%$ Cu (Fig. 4c). Although dense dislocations form in matrix, the energy dispersive spectroscopy (EDS) mapping shows all the elements are homogeneously distributed in medium-magnification area.

Furthermore, HADDF-STEM image and strain mapping of $\text{Pb}_{1.02}\text{Se}_{0.72}\text{Te}_{0.20}\text{S}_{0.08}-0.3\%$ Cu display more details on the dislocation and the strain distribution (Fig. 5). One clear edge dislocation can be witnessed (Fig. 5a), and the corresponding Burgers vector $\mathbf{b} = 1/2[01\bar{1}]$ is defined by Burgers circuit (Fig. 5b). The geometric phase analysis (GPA) results (Fig. 5c, d) demonstrate that edge dislocation could cause obvious linear strain field in lattice along both strain tensor ϵ_{xx} and ϵ_{yy} . The EDS mapping results (Fig. 5e and Supplementary Fig. 7) show that there is Cu-rich area around the edge dislocation, which indicates the role of Cu interstitials to promote dislocation formation. Another screw dislocation is presented with a Burgers vector $\mathbf{b} = 1/3[111]$ (Fig. 5f). Moreover, the GPA results of this screw dislocation also unclosed strong strain fields (Fig. 5g, h). These strain fields induced by both edge and screw dislocations can reinforce the phonon scattering

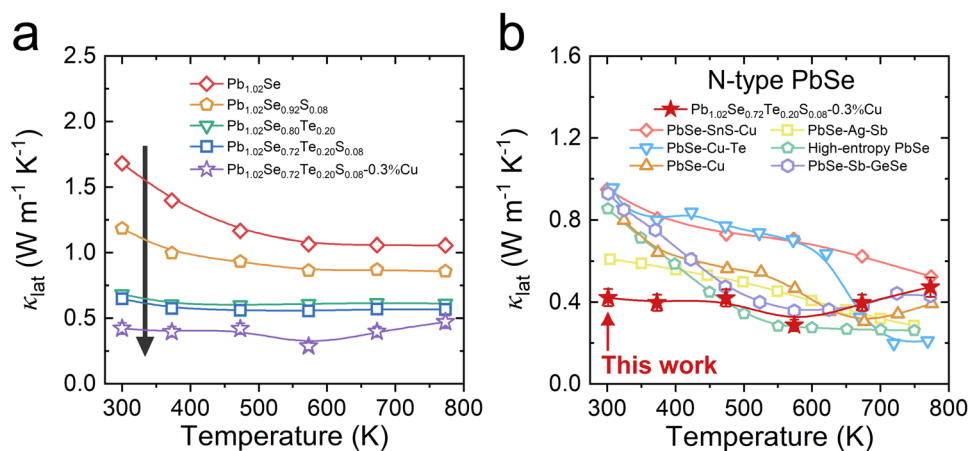


Fig. 2 | Optimization and comparison of lattice thermal conductivity. **a** Optimization of temperature-dependent lattice thermal conductivity from $\text{Pb}_{1.02}\text{Se}$ to $\text{Pb}_{1.02}\text{Se}_{0.72}\text{Te}_{0.20}\text{S}_{0.08}-0.3\%\text{Cu}$. **b** Comparison of lattice thermal conductivity in *n*-type PbSe. Error bars are $\pm 10\%$.

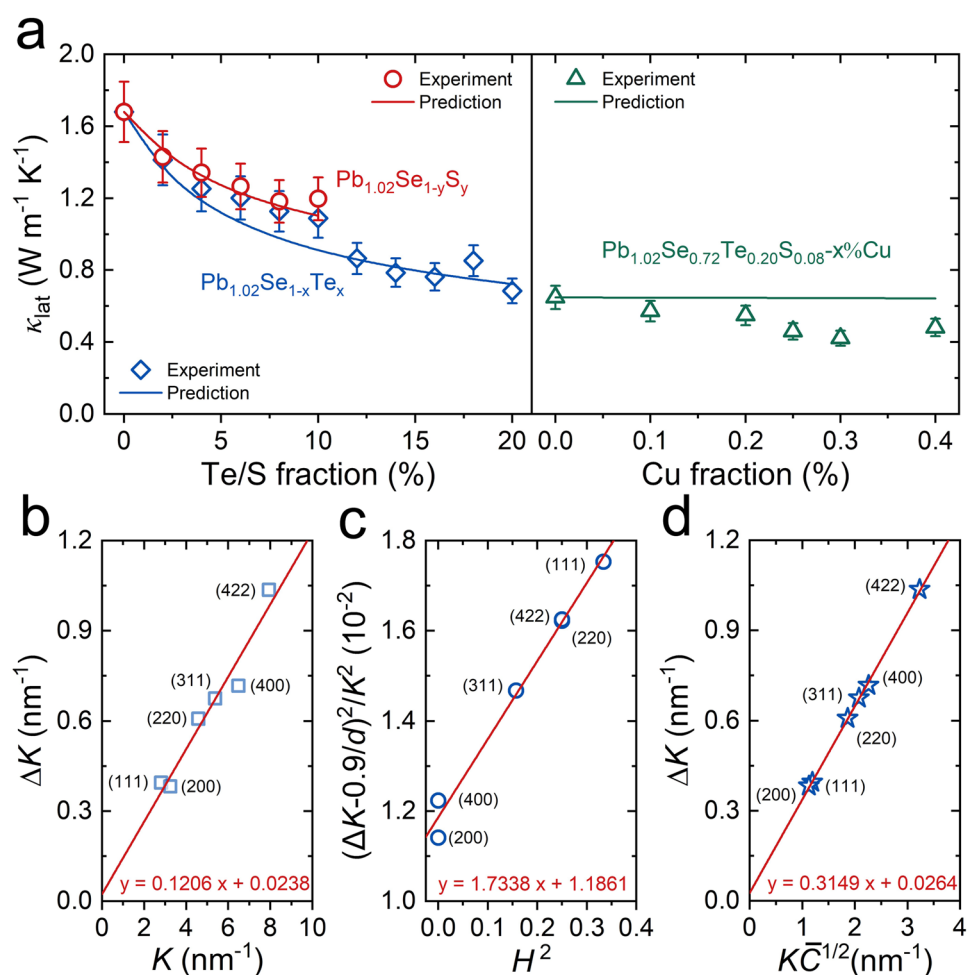


Fig. 3 | Lattice thermal conductivity of model prediction and estimation of dislocation density in $\text{Pb}_{1.02}\text{Se}_{0.72}\text{Te}_{0.20}\text{S}_{0.08}-0.3\%\text{Cu}$ by MWH method. **a** Room-temperature lattice thermal conductivity as a function of Te, S, and Cu content for

$\text{Pb}_{1.02}\text{Se}_{1-x}\text{Te}_x$ ($x = 0.20$), $\text{Pb}_{1.02}\text{Se}_{1-y}\text{S}_y$ ($y = 0-0.10$), and $\text{Pb}_{1.02}\text{Se}_{0.72}\text{Te}_{0.20}\text{S}_{0.08}-x\%\text{Cu}$ ($x = 0-0.40$). The solid curve is the prediction by Callaway model. Error bars are $\pm 10\%$. **b** Plot of $\Delta K - K$. **c** Plot of $(\Delta K - 0.9/d)^2/K^2 - H^2$. **d** Plot of $\Delta K - K\bar{C}^{1/2}$.

to largely reduce the lattice thermal conductivity. Notably, the screw dislocation could play a stronger role to scatter phonon transport than edge dislocation due to its larger-scale strain field. The different roles between edge and screw dislocations could provide new and detailed understandings of dislocation to scatter phonon, and can also provide reference for importing dislocation in thermoelectric materials.

Electrical transport properties in $\text{Pb}_{1.02}\text{Se}_{0.72}\text{Te}_{0.20}\text{S}_{0.08}-x\%\text{Cu}$ ($x = 0-0.40$)

Although dense dislocations are imported in $\text{Pb}_{1.02}\text{Se}_{0.72}\text{Te}_{0.20}\text{S}_{0.08}-x\%\text{Cu}$ ($x = 0-0.40$), the matrix can also maintain high electrical transport performance. With increasing Cu interstitial content in $\text{Pb}_{1.02}\text{Se}_{0.72}\text{Te}_{0.20}\text{S}_{0.08}-x\%\text{Cu}$ ($x = 0-0.40$), the

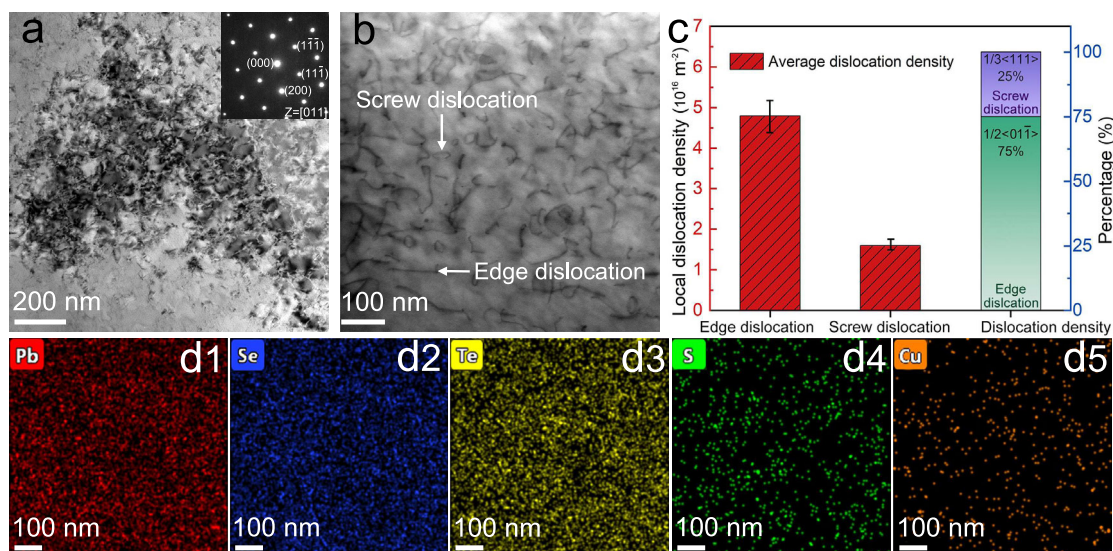


Fig. 4 | Dense dislocations in $\text{Pb}_{1.02}\text{Se}_{0.72}\text{Te}_{0.20}\text{S}_{0.08}-0.3\%\text{Cu}$. **a** Low-magnification TEM image, the insert is the electron diffraction pattern along [011]. **b** Medium-magnification STEM ABF image. **c** Estimation of dislocation density and fraction. Error bars are $\pm 10\%$. **d1–d5** EDS mapping of Pb, Se, Te, S, and Cu in **b**.

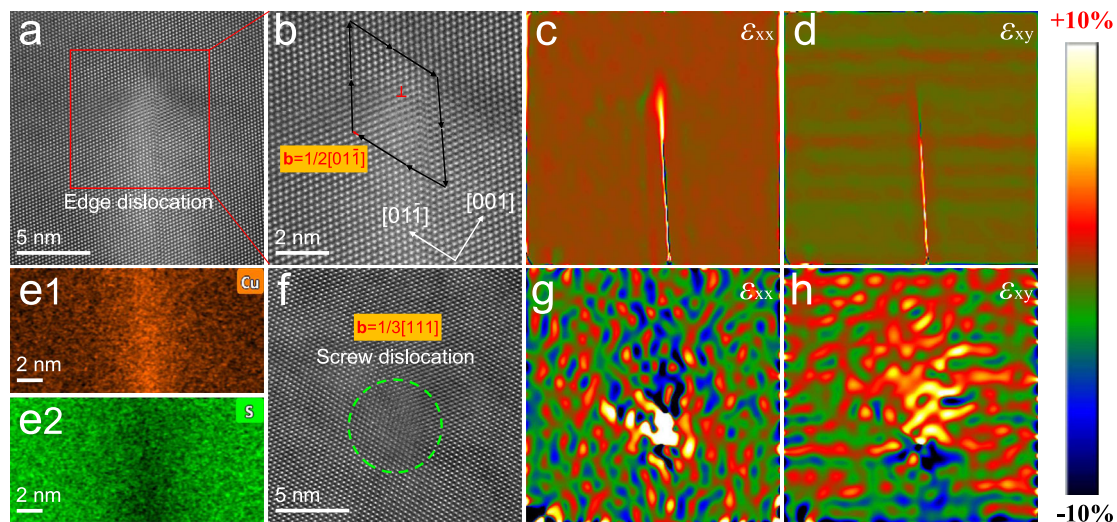


Fig. 5 | The feature of the edge dislocation and screw dislocation in $\text{Pb}_{1.02}\text{Se}_{0.72}\text{Te}_{0.20}\text{S}_{0.08}-0.3\%\text{Cu}$. **a** HAADF-STEM image of one edge dislocation. **b** Burgers vector of the corresponding region of **a**. **c, d** GPA strain analysis of **a**. **e1, e2** EDS mapping of Cu and S at edge dislocation. **f** HRTEM HADDF image of one screw dislocation. **g, h** GPA strain analysis of **f**.

electrical conductivity continues to rise because Cu interstitial doping can release extra free electrons into matrix (Fig. 6a). The enhanced electrical conductivity is consistent with the lowered absolute value of Seebeck coefficient (Fig. 6b). Moreover, the down-and-up tendency in temperature-dependent electrical conductivity and Seebeck coefficient indicates the dynamic doping behavior of Cu interstitials in lead chalcogenides as proved in our previous works^{20,42,43}. Benefiting from the Cu interstitial doping, the power factor in $\text{Pb}_{1.02}\text{Se}_{0.72}\text{Te}_{0.20}\text{S}_{0.08}-x\%\text{Cu}$ ($x = 0-0.40$) is obviously enhanced in the whole-temperature range. The maximum power factor is enhanced by double, from $7.73 \mu\text{W cm}^{-1} \text{K}^2$ in $\text{Pb}_{1.02}\text{Se}_{0.72}\text{Te}_{0.20}\text{S}_{0.08}$ to $14.6 \mu\text{W cm}^{-1} \text{K}^2$ in $\text{Pb}_{1.02}\text{Se}_{0.72}\text{Te}_{0.20}\text{S}_{0.08}-0.3\%\text{Cu}$ (Fig. 6c). Here, the weighted carrier mobility (μ_w) is introduced to evaluate the contribution of Cu atom to electrical transport properties. The parameter μ_w can be calculated with measured electrical conductivity and Seebeck coefficient

by the following relationships⁴⁴:

$$\mu_w = \frac{3\sigma}{8\pi e F_0(\eta)} \left(\frac{h^2}{2m_e k_B T} \right)^{3/2} \quad (3)$$

$$F_n(\eta) = \int_0^\infty \frac{x^n}{1+e^{x-\eta}} dx \quad (4)$$

$$S = \pm \frac{k_B}{e} \left(\frac{(r+5/2)F_{r+3/2}(\eta)}{(r+3/2)F_{r+1/2}(\eta)} - \eta \right) \quad (5)$$

where e , h , m_e , and k_B donate the unite charge, Planck constant, electron mass, and the Boltzmann constant, respectively. $F_n(\eta)$ is the Fermi integral, η is reduced Fermi level, and r is the scattering factor and equals

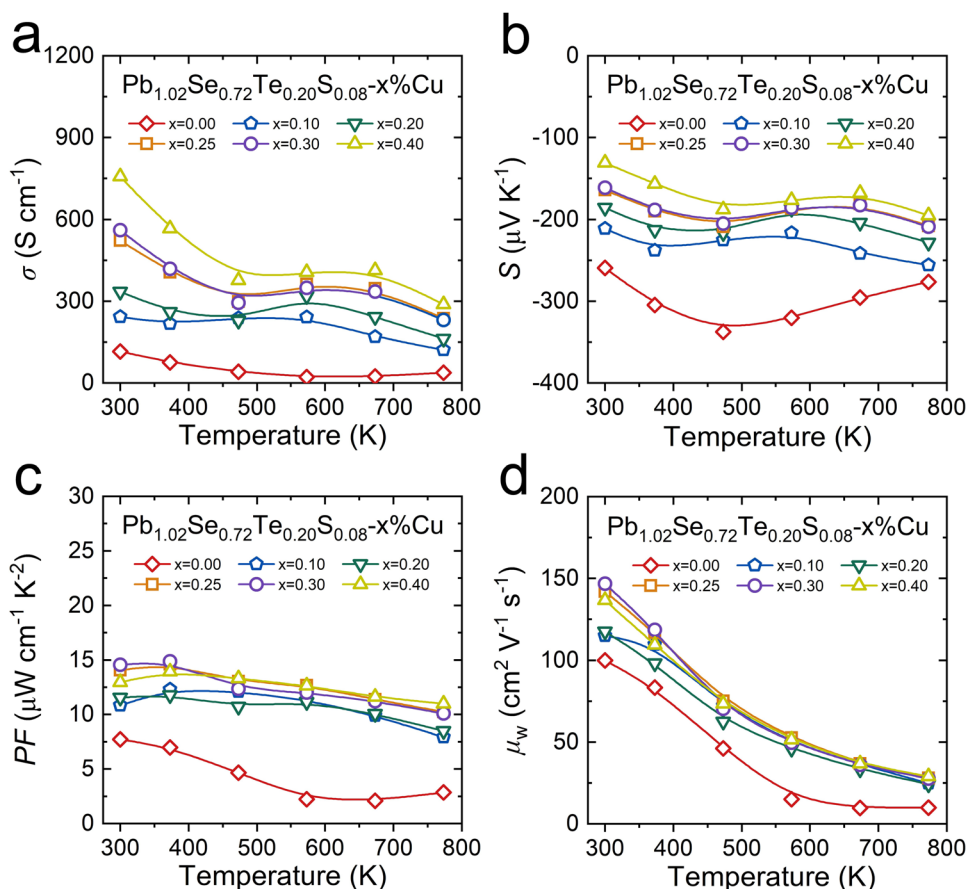


Fig. 6 | Temperature-dependent electrical transport properties in $\text{Pb}_{1.02}\text{Se}_{0.72}\text{Te}_{0.20}\text{S}_{0.08-x}\text{Cu}$. **a** Electrical conductivity. **b** Seebeck coefficient. **c** Power factor. **d** Weighted carrier mobility (μ_w).

$-1/2$ when the acoustic scattering mechanism dominates. The temperature-dependent μ_w of $\text{Pb}_{1.02}\text{Se}_{0.72}\text{Te}_{0.20}\text{S}_{0.08-x}\text{Cu}$ ($x = 0-0.40$) (Fig. 6d) shows that Cu interstitial doping can well promote μ_w and a maximum value of $146.90 \text{ cm}^2 \text{ V}^{-1} \text{ s}^{-1}$ is obtained in $\text{Pb}_{1.02}\text{Se}_{0.72}\text{Te}_{0.20}\text{S}_{0.08-0.3}\text{Cu}$ at room temperature, which is the origin of the enhanced power factor.

Thermal transport properties and ZT value in $\text{Pb}_{1.02}\text{Se}_{0.72}\text{Te}_{0.20}\text{S}_{0.08-x}\text{Cu}$ ($x = 0-0.40$)

Owing to the increased electrical conductivity, the total thermal conductivity in $\text{Pb}_{1.02}\text{Se}_{0.72}\text{Te}_{0.20}\text{S}_{0.08-x}\text{Cu}$ ($x = 0-0.40$) undergoes an increasing tendency after Cu interstitial doping (Fig. 7a). With electronic thermal conductivity (Supplementary Fig. 8), the lattice thermal conductivity in $\text{Pb}_{1.02}\text{Se}_{0.72}\text{Te}_{0.20}\text{S}_{0.08-x}\text{Cu}$ ($x = 0-0.40$) is calculated out (Fig. 7b). Moreover, benefiting from the dense dislocations in $\text{Pb}_{1.02}\text{Se}_{0.72}\text{Te}_{0.20}\text{S}_{0.08-x}\text{Cu}$ ($x = 0-0.40$) as discussed above, the lattice thermal conductivity can be further suppressed with Cu interstitial doping. To evaluate the synergistic role of Cu interstitial doping in $\text{Pb}_{1.02}\text{Se}_{0.72}\text{Te}_{0.20}\text{S}_{0.08-x}\text{Cu}$ ($x = 0-0.40$), the temperature-dependent ratio of weighted carrier mobility to lattice thermal conductivity (μ_w/k_{lat}) is calculated out (Fig. 7c). The temperature-dependent μ_w/k_{lat} values show decreasing tendency with rising temperature, but obtain large enhancement after Cu interstitial doping. Finally, the ZT values are distinctly enhanced in $\text{Pb}_{1.02}\text{Se}_{0.72}\text{Te}_{0.20}\text{S}_{0.08-x}\text{Cu}$ ($x = 0-0.40$) (Fig. 7d). Notably, the room-temperature ZT value of $\text{Pb}_{1.02}\text{Se}_{0.72}\text{Te}_{0.20}\text{S}_{0.08-0.3}\text{Cu}$ can reach at 0.62, indicating potential application of PbSe-based thermoelectric near room temperature. Additionally, the cycle test results (Supplementary Fig. 9) further demonstrate a good repeatability and high reliability of high-performance $\text{Pb}_{1.02}\text{Se}_{0.72}\text{Te}_{0.20}\text{S}_{0.08-0.3}\text{Cu}$.

The room-temperature thermoelectric properties between $\text{Pb}_{1.02}\text{Se}_{0.72}\text{Te}_{0.20}\text{S}_{0.08-0.3}\text{Cu}$ in this work and other n -type PbSe-based samples with dislocation are compared (Fig. 8a, b). It is found that all the samples present low lattice thermal conductivity, proving the positive role of dislocation to scatter phonon. Interestingly, the Cu interstitial-induced dislocation in n -type PbSe can result in better electrical transport properties than that in samples with Pb vacancy-induced dislocation. This might be closely related to the local carrier types (electron or hole) near different dislocations. Specifically, the interstitial-induced dislocation is dominated by donor electron that is beneficial to n -type sample, but the cation vacancy-induced dislocation contains local hole carrier, which could cause energy barrier for electrical transport in n -type thermoelectric materials. Owing to much higher dislocation density in $\text{Pb}_{1.02}\text{Se}_{0.72}\text{Te}_{0.20}\text{S}_{0.08-0.3}\text{Cu}$, this work can obtain very low lattice thermal conductivity and simultaneously maintain relatively high power factor, which is conducive to the improvement of ZT value at room temperature (Fig. 8c) and enhance the ZT_{ave} value in 300–573 K. Compared with other state-of-the-art n -type PbSe, $\text{Pb}_{1.02}\text{Se}_{0.72}\text{Te}_{0.20}\text{S}_{0.08-0.3}\text{Cu}$ presents a superior ZT value at 300–573 K (Fig. 8d). Moreover, its ZT_{RT} and ZT_{ave} value at 300–573 K can reach up to 0.62 and 0.90, respectively, outperforming other reported high-performance n -type PbSe-based thermoelectric materials, such as $ZT_{\text{RT}} - 0.58$ and $ZT_{\text{ave}} - 0.86$ in PbSe-SnS-Cu^{20} , $ZT_{\text{RT}} - 0.48$ and $ZT_{\text{ave}} - 0.86$ in PbSe-Cd-Cu^{30} , $ZT_{\text{RT}} - 0.35$ and $ZT_{\text{ave}} - 0.75$ in PbSe-Cu-Te^{29} , $ZT_{\text{RT}} - 0.33$ and $ZT_{\text{ave}} - 0.72$ in PbSe-Cu^{22} , $ZT_{\text{RT}} - 0.17$ and $ZT_{\text{ave}} - 0.52$ in $\text{PbSe-Br-Cu}_2\text{Se}^{19}$, $ZT_{\text{RT}} - 0.10$ and $ZT_{\text{ave}} - 0.40$ in high-entropy PbSe³². More importantly, this high ZT_{ave} value in $\text{Pb}_{1.02}\text{Se}_{0.72}\text{Te}_{0.20}\text{S}_{0.08-0.3}\text{Cu}$ is comparable with the thermoelectric performance in typical n -type Bi_2Te_3 -based materials, including commercial

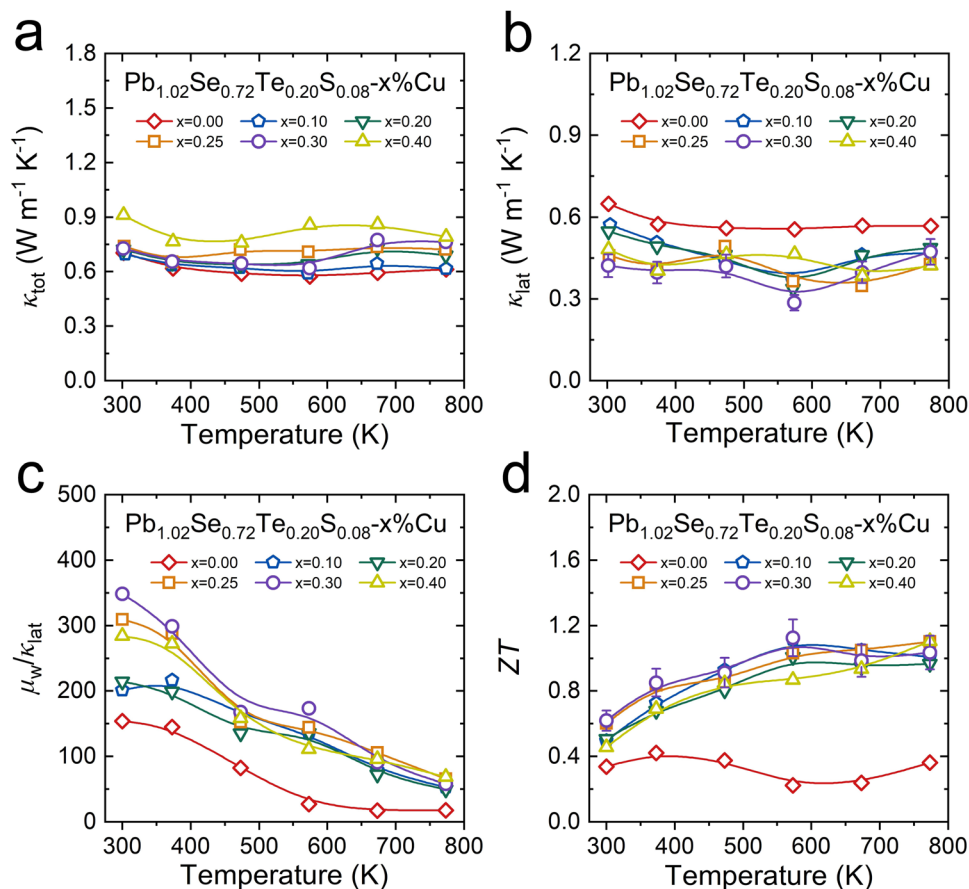


Fig. 7 | Temperature-dependent thermal conductivity and ZT values in $\text{Pb}_{1.02}\text{Se}_{0.72}\text{Te}_{0.20}\text{S}_{0.08}\text{-x}\% \text{Cu}$. **a** Total thermal conductivity. **b** Lattice thermal conductivity. Error bars are $\pm 10\%$. **c** Ratio of weighted carrier mobility to lattice thermal conductivity. **d** ZT values. Error bars are $\pm 10\%$.

$\text{Bi}_2\text{Te}_{2.5}\text{Se}_{0.5}$ ⁴⁵, $\text{Bi}_2\text{Te}_{2.7}\text{Se}_{0.3} + 1\text{wt}\% \text{Bi}_2\text{S}_3$ ⁴⁶, and $\text{Bi}_2\text{Te}_3 + 1\text{wt}\% \text{Ru}$ ⁴⁷ (Supplementary Fig. 10). The present high near-room-temperature thermoelectric performance indicates that $\text{Pb}_{1.02}\text{Se}_{0.72}\text{Te}_{0.20}\text{S}_{0.08}\text{-0.3}\% \text{Cu}$ has great potential for thermoelectric cooling applications at low-medium temperatures.

Discussion

In summary, high-density dislocation is realized in $\text{Pb}_{1.02}\text{Se}_{0.72}\text{Te}_{0.20}\text{S}_{0.08}\text{-0.3}\% \text{Cu}$ through heavy alloying and interstitial doping. Such dense dislocations can form dislocation networks and largely reduce the lattice thermal conductivity in the whole-temperature range. The room-temperature and minimal lattice thermal conductivity can be suppressed to $0.42 \text{ W m}^{-1} \text{ K}^{-1}$ and $0.29 \text{ W m}^{-1} \text{ K}^{-1}$ in $\text{Pb}_{1.02}\text{Se}_{0.72}\text{Te}_{0.20}\text{S}_{0.08}\text{-0.3}\% \text{Cu}$. Additionally, Cu interstitials not only promotes dislocation formation to intensify phonon scattering but also works as donor dopant to optimize carrier transport properties. The resultant reduced thermal conductivity and preserved electrical transport properties finally contribute to a high ZT_{ave} of 0.96 in *n*-type $\text{Pb}_{1.02}\text{Se}_{0.72}\text{Te}_{0.20}\text{S}_{0.08}\text{-0.3}\% \text{Cu}$ at low-medium temperatures (300–773 K), which mainly originates from its enhanced performance at low temperature range (300–573 K). The work provides a new approach to enhance the thermoelectric performance in lead chalcogenides at low-medium temperatures, and the strategy of heavy alloying and interstitial doping to produce dense dislocations can be also extended to other thermoelectric semiconductors.

Methods

Synthesis

High-purity raw materials, Pb bulk (99.999%), Se particles (99.999%), Te bulk (99.999%), S powders (99.99%), and Cu wires (99.99%) with stoichiometric composition were weighted and flame-sealed in silica

tubes at a residual pressure below 10^{-4} Torr, slowly heated to 1323 K in 12 h and kept at this temperature for 6 h followed by furnace cooling to room temperature. The obtained ingots were ground into powders and densified by hot-pressing furnace (OTF-1700X-RHP4) at 773 K for 40 min in a $\Phi 15$ mm cylindrical die under an axial compressive stress of 50 MPa in vacuum, resulting in highly densified disk-shaped samples. Finally, the disk-shaped samples were annealed at 773 K for 6 h.

Structural characterization

The phase identification was characterized through powder X-ray diffraction with Cu $K\alpha$ ($\lambda = 1.5418 \text{ \AA}$) radiation in a reflection geometry operating at 40 kV and 40 mA. The lattice parameters were calculated and refined by using the software package, which named “Materials Analysis using Diffraction (MAUD)”. The transmission electron microscopy (TEM) and high-resolution TEM (HRTEM) image as well as the scanning transmission electron microscopy (AC-STEM) HAADF image were conducted on a spherical aberration corrected Transmission Electron Microscope (Thermalfisher Titan Themis Z). TEM samples are prepared by focused ion beam (FIB) method on Thermalfisher Scios 2.

Thermoelectric transport properties measurements

The obtained highly densified hot-pressing (HP) processed disk-shaped samples were cut into bars with dimensions around $12 \times 4 \times 4$ mm to measure electrical conductivity (σ) and Seebeck coefficient (S) from 300 to 773 K by using a CTA equipment (Cryoall, China) under a low-pressure helium atmosphere. The HP disk-shaped samples were cut and polished into a square with sizes of 8×8 mm and 1.5 mm thickness for thermal diffusivity (D) measurements. The samples were coated with a thin-graphite layer to minimize errors from the emissivity method in LFA-467 (Netzsch,

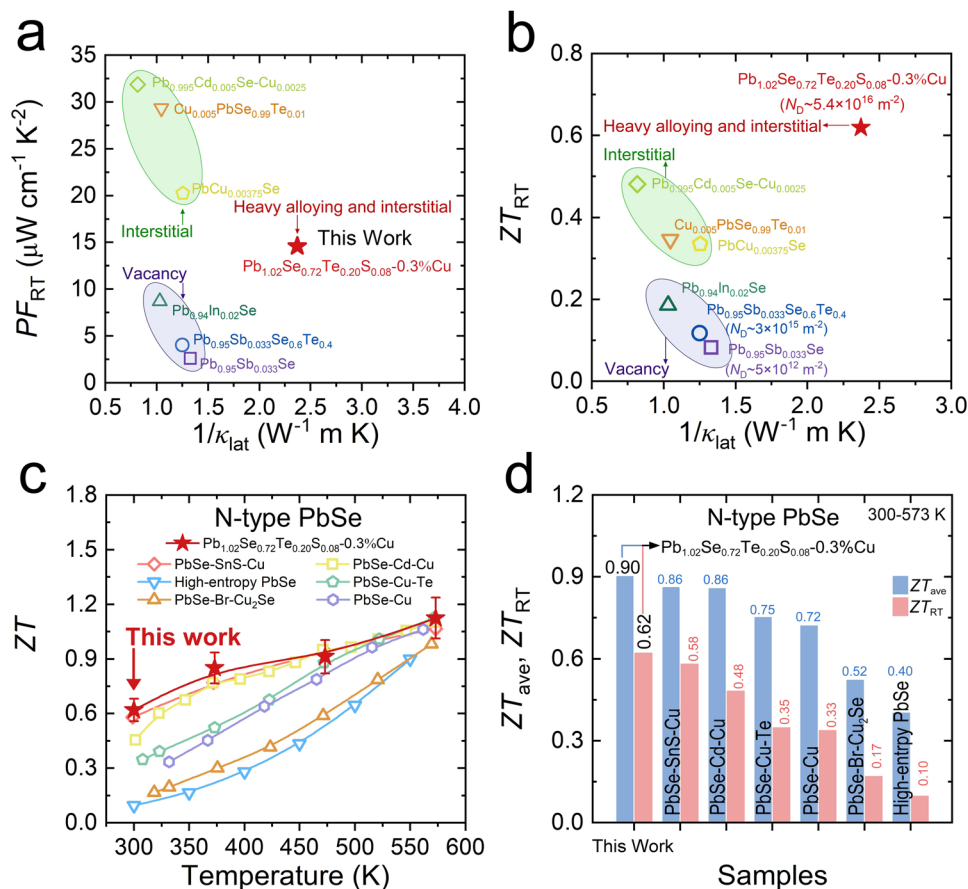


Fig. 8 | Comparisons of thermoelectric transport performance in n-type PbSe-based thermoelectric materials. a PF value as a function of $1/\kappa_{lat}$ at room temperature. **b** ZT value as a function of $1/\kappa_{lat}$ at room temperature. **c** Temperature-

dependent ZT value. Error bars are $\pm 10\%$. **d** ZT_{ave} value at 300–573 K and ZT value at room temperature.

Germany) and CLA-1000 (Cryoall, China) instruments. The sample density (ρ) was determined using the dimensions and mass of the samples. The specific heat capacity (C_p) was calculated by the Debye model. The thermal diffusivity data was analyzed using a Cowan model with pulse correction.

Data availability

The authors declare that the data supporting the findings of this study are available on reasonable request.

References

- Qin, B. et al. Power generation and thermoelectric cooling enabled by momentum and energy multiband alignments. *Science* **373**, 556–561 (2021).
- Tang, X., Li, Z., Liu, W., Zhang, Q. & Uher, C. A comprehensive review on Bi_2Te_3 -based thin films: thermoelectrics and beyond. *Interdiscip. Mater.* **1**, 88–115 (2022).
- Fan, Y. & Tan, G. Ferroelectric engineering advances thermoelectric materials. *Mater. Lab.* **1**, 220008 (2022).
- Zhang, F., Wu, D. & He, J. The roles of grain boundaries in thermoelectric transports. *Mater. Lab.* **1**, 220012 (2022).
- Xiao, Y. Routes to High-ranged Thermoelectric Performance. *Mater. Lab.* **1**, 220025 (2022).
- Liu, Z. Challenges for thermoelectric power generation: from a material perspective. *Mater. Lab.* **1**, 220003 (2022).
- Qin, B. & Zhao, L.-D. Carriers: the Less, the Faster. *Mater. Lab.* **1**, 220004 (2022).
- Pei, Y. et al. Convergence of electronic bands for high performance bulk thermoelectrics. *Nature* **473**, 66–69 (2011).
- Zhao, L.-D. et al. All-scale hierarchical thermoelectrics: MgTe in PbTe facilitates valence band convergence and suppresses bipolar thermal transport for high performance. *Energy Environ. Sci.* **6**, 3346–3355 (2013).
- Heremans, J. P. et al. Enhancement of thermoelectric efficiency in PbTe by distortion of the electronic density of states. *Science* **321**, 554–557 (2008).
- Zhang, Q. et al. Enhancement of thermoelectric figure-of-merit by resonant states of aluminium doping in lead selenide. *Energy Environ. Sci.* **5**, 5246–5251 (2012).
- Androulakis, J. et al. Thermoelectrics from abundant chemical elements: high-performance nanostructured PbSe-PbS. *J. Am. Chem. Soc.* **133**, 10920–10927 (2011).
- Zhao, L.-D. et al. Thermoelectrics with earth abundant elements: high performance p-type PbS nanostructured with SrS and CaS. *J. Am. Chem. Soc.* **134**, 7902–7012 (2012).
- Pei, Y., May, A. F. & Snyder, G. J. Self-tuning the carrier concentration of PbTe/Ag₂Te composites with excess ag for high thermoelectric performance. *Adv. Energy Mater.* **1**, 291–296 (2011).
- He, J. et al. Strong phonon scattering by layer structured PbSnS₂ in PbTe based thermoelectric materials. *Adv. Mater.* **24**, 4440–4444 (2012).
- Girard, S. N. et al. High performance Na-doped PbTe-PbS thermoelectric materials: electronic density of states modification and shape-controlled nanostructures. *J. Am. Chem. Soc.* **133**, 16588–16597 (2011).
- Qian, X. et al. Synergistically optimizing interdependent thermoelectric parameters of n-type PbSe through alloying CdSe. *Energy Environ. Sci.* **12**, 1969–1978 (2019).

18. Xu, F. et al. Effects of La doping induced carrier concentration regulation and band structure modification on thermoelectric properties of PbSe. *Scr. Mater.* **208**, 114360 (2022).
19. Zhou, C. et al. High-Performance n-Type PbSe-Cu₂Se Thermoelectrics through Conduction Band Engineering and Phonon Softening. *J. Am. Chem. Soc.* **140**, 15535–15545 (2018).
20. Xiao, Y. et al. Ultrahigh carrier mobility contributes to remarkably enhanced thermoelectric performance in n-type PbSe. *Energy Environ. Sci.* **15**, 346–355 (2022).
21. Xiao, Y. et al. Rationally optimized carrier effective mass and carrier density leads to high average ZT value in n-type PbSe. *J. Mater. Chem. A* **9**, 23011–23018 (2021).
22. You, L. et al. Boosting the thermoelectric performance of PbSe through dynamic doping and hierarchical phonon scattering. *Energy Environ. Sci.* **11**, 1848–1858 (2018).
23. Zhou, C. & Chung, I. Nanoscale defect structures advancing high performance n-type PbSe thermoelectrics. *Coord. Chem. Rev.* **421**, 213437 (2020).
24. Luo, Z. et al. Soft phonon modes from off-center Ge atoms lead to ultralow thermal conductivity and superior thermoelectric performance in n-type PbSe-GeSe. *Energy Environ. Sci.* **11**, 3220–3230 (2018).
25. Kim, M. S., Lee, W. J., Cho, K. H., Ahn, J. P. & Sung, Y. M. Spinodally decomposed PbSe-PbTe Nanoparticles for high-performance thermoelectrics: enhanced phonon scattering and unusual transport behavior. *ACS Nano* **10**, 7197–7207 (2016).
26. Chen, Z. et al. Vacancy-induced dislocations within grains for high-performance PbSe thermoelectrics. *Nat. Commun.* **8**, 13828 (2017).
27. Hong, M., Chen, Z.-G., Matsumura, S. & Zou, J. Nano-scale dislocations induced by self-vacancy engineering yielding extraordinary n-type thermoelectric Pb_{0.96-y}In_ySe. *Nano Energy* **50**, 785–793 (2018).
28. Xin, J. et al. Mg vacancy and dislocation strains as strong phonon scatterers in Mg₂Si_{1-x}Sb_x thermoelectric materials. *Nano Energy* **34**, 428–436 (2017).
29. Zhang, D. et al. ds-block element-enabled cooperative regulation of electrical and thermal transport for extraordinary N- and P-type PbSe thermoelectrics near room temperature. *Chem. Mater.* **34**, 1862–1874 (2022).
30. Zhou, C. et al. Exceptionally high average power factor and thermoelectric figure of merit in n-type PbSe by the dual incorporation of Cu and Te. *J. Am. Chem. Soc.* **142**, 15172–15186 (2020).
31. Duan, S. et al. Improved thermoelectric performance in PbSe-AgSbSe₂ by manipulating the spin-orbit coupling effects. *Nano Energy* **78**, 105232 (2020).
32. Jiang, B. et al. High-entropy-stabilized chalcogenides with high thermoelectric performance. *Science* **371**, 830–834 (2021).
33. Cahill, D. G., Watson, S. K. & Pohl, R. O. Lower limit to the thermal conductivity of disordered crystals. *Phys. Rev. B* **46**, 6131–6140 (1992).
34. Lin, S., Li, W. & Pei, Y. Thermally insulative thermoelectric argyrodites. *Mater. Today* **48**, 198–213 (2021).
35. Berges, T. et al. Considering the role of ion transport in diffusion-dominated thermal conductivity. *Adv. Energy Mater.* **12**, 2200717 (2022).
36. Ungár, T. & Borbély, A. The effect of dislocation contrast on x-ray line broadening: A new approach to line profile analysis. *Appl. Phys. Lett.* **69**, 3173–3175 (1996).
37. Ungár, T., Ott, S., Sanders, P. G., Borbély, A. & Weertman, J. R. Dislocations, grain size and planar faults in nanostructured copper determined by high resolution X-ray diffraction and a new procedure of peak profile analysis. *Acta Mater.* **46**, 3693–3699 (1998).
38. Ungar, T., Dragomir, I., Revesz, A. & Borbély, A. The contrast factors of dislocations in cubic crystals: the dislocation model of strain anisotropy in practice. *J. Appl. Crystallogr.* **32**, 992–1002 (1999).
39. Zhou, C. et al. Defect engineering for high-performance n-type PbSe thermoelectrics. *J. Am. Chem. Soc.* **140**, 9282–9290 (2018).
40. Chen, Z. et al. Lattice dislocations enhancing thermoelectric PbTe in addition to band convergence. *Adv. Mater.* **29**, 1606768 (2017).
41. Yu, Y. et al. Ag-segregation to dislocations in PbTe-based thermoelectric materials. *ACS Appl. Mater. Interfaces* **10**, 3609–3615 (2018).
42. Xiao, Y. et al. High-ranged ZT value promotes thermoelectric cooling and power generation in n-Type PbTe. *Adv. Energy Mater.* **12**, 2200204 (2022).
43. Qin, Y. et al. Contrasting Cu roles lead to high ranged thermoelectric performance of PbS. *Adv. Funct. Mater.* **31**, 2102185 (2021).
44. Snyder, G. J. et al. Weighted mobility. *Adv. Mater.* **32**, e2001537 (2020).
45. Pan, Y., Wei, T., Cao, Q. & Li, J. Mechanically enhanced p- and n-type Bi₂Te₃-based thermoelectric materials reprocessed from commercial ingots by ball milling and spark plasma sintering. *Mater. Sci. Eng. B* **197**, 75–81 (2015).
46. Zhu, Y. et al. Ultralow lattice thermal conductivity and enhanced power generation efficiency realized in Bi₂Te_{2.7}Se_{0.3}/Bi₂S₃ nanocomposites. *Acta Mater.* **218**, 117230 (2021).
47. Zhu, Y. et al. Simultaneous enhancement of thermoelectric performance and mechanical properties in Bi₂Te₃ via Ru compositing. *Chem. Eng. J.* **407**, 126407 (2021).

Acknowledgements

We acknowledge the support from the National Key Research and Development Program of China (2018YFA0702100), National Natural Science Foundation of China (52172236), Fundamental Research Funds for the Central Universities (xtr042021007), Top Young Talents Programme of Xi'an Jiaotong University, National Science Fund for Distinguished Young Scholars (51925101). Y.X. would like to acknowledge the strong support from Instrumental Analysis Center of Xi'an Jiaotong University.

Author contributions

Y.X. and L.X. designed the experiments, synthesized the samples, carried out the transport property measurements and wrote the manuscript. L.X., S.W., and D.W. performed the thermal transport measurement. B.C. performed the transmission electron microscope observation. Y.X., X.D., and L.-D.Z. discussed the results and revised this manuscript.

Competing interests

The authors declare no competing interests.

Additional information

Supplementary information The online version contains supplementary material available at <https://doi.org/10.1038/s41467-022-34227-3>.

Correspondence and requests for materials should be addressed to Yu Xiao, Bo Cui or Li-Dong Zhao.

Peer review information *Nature Communications* thanks Yoshikazu Mizuguchi and the other anonymous reviewer(s) for their contribution to the peer review of this work.

Reprints and permissions information is available at <http://www.nature.com/reprints>

Publisher's note Springer Nature remains neutral with regard to jurisdictional claims in published maps and institutional affiliations.

Open Access This article is licensed under a Creative Commons Attribution 4.0 International License, which permits use, sharing, adaptation, distribution and reproduction in any medium or format, as long as you give appropriate credit to the original author(s) and the source, provide a link to the Creative Commons license, and indicate if changes were made. The images or other third party material in this article are included in the article's Creative Commons license, unless indicated otherwise in a credit line to the material. If material is not included in the article's Creative Commons license and your intended use is not permitted by statutory regulation or exceeds the permitted use, you will need to obtain permission directly from the copyright holder. To view a copy of this license, visit <http://creativecommons.org/licenses/by/4.0/>.

© The Author(s) 2022